Estimating dry fracture weaknesses and pressure relaxation related parameter in reservoirs containing aligned cracks

Huaizhen Chen*, Junxiao Li, and Kristopher A. Innanen

ABSTRACT

Based on a model of attenuative cracked rock, we derive a simplified and frequency-dependent stiffness matrix in the case that the rock contains aligned partially saturated cracks, and in the stiffness matrix we also involve the effect of pressure relaxation that is a sensitive fluid factor directly influenced by fluid viscosity and saturation. Using perturbation in stiffness matrix for an interface separating two attenuative cracked media and relationship between scattering potential and reflection coefficient, we propose a linearized reflection coefficient in the case of P-wave incidence and P-wave scattering, which is a azimuth- and frequency-dependent function of dry rock elastic property, dry fracture weaknesses and pressure relaxation related parameter. Using difference in the reflection coefficients between azimuthal angles, we derive an expression of Quasi-difference in Elastic Impedance ($Q\delta\mathrm{EI}$) that is mainly affected by dry fracture weaknesses and pressure relaxation related parameter. Using the derived $Q\delta\mathrm{EI}$, we establish an inversion approach of employing frequency-dependent differences in seismic amplitudes to estimate dry fracture weaknesses and pressure relaxation related parameter. Applying the established approach to synthetic datasets, we conclude the approach can obtain acceptable inversion results of dry fracture weaknesses and pressure relaxation related parameter in the case of generated synthetic data containing a moderate signal-to-noise ratio (SNR). Test on a real data set reveals that the inversion results of dry fracture weaknesses provide a reliable tool in fracture prediction, and the estimated pressure relaxation related parameter appear as an additional proof for the discrimination of fluids in cracks.

INTRODUCTION

Seismic wave propagation in porous and cracked rocks exhibits both anisotropy and attenuation. In the case of porous rocks containing a set of vertically parallel cracks, an effective model is proposed by Hudson et al. (1996) to calculate complex stiffness matrices of porous and cracked rocks, in which two frequency-dependent complex variables $\widetilde{U_{11}}$ and $\widetilde{U_{33}}$ are defined to describe how fluid parameters (e.g. fluid viscosity and bulk modulus) and crack properties (e.g. crack aspect ratio) affect the complex stiffness matrix. The effective model reveals that reflection amplitude of seismic wave varies with frequency (Gurevich, 2003; Chapman et al., 2006; Carcione, 2000, 2007), from which pressure relaxation time that is sensitive to fluid parameters is proposed. In the present study, we will combine characteristics of seismic reflection amplitude variations with offset/incidence angle ($\mathrm{AVO}/\mathrm{AVA}$), azimuthal angle ($\mathrm{AVAZ}$), and frequency ($\mathrm{AVAZF}$) to implement the prediction of fractures and fluids in hydrocarbon reservoirs.

Many fluid factors are currently established for indicate types of fluids in reservoirs. Lamé constants, λ and μ, and their products with density (Lamé impedance), $\lambda\rho$ and $\mu\rho$, are directly employed to discriminate hydrocarbon reservoirs because λ is sensitive to fluid types and μ is only related to dry rock framework (Goodway, 2001; Zimmer, 2003). Based

on Boit-Gassmann theory, Russell et al. (2003, 2011) propose a mixed fluid/rock term that depends on fluids, rock porosity and minerals; however the fluid/rock term is dominantly affected by fluid component. In the case of hydrocarbon reservoirs containing aligned cracks/fractures, a quantity combining P- and S-wave velocity ratio and fracture weaknesses is constructed to identify fluids in cracks/fractures (Schoenberg and Sayers, 1995; Bakulin et al., 2000). Following Russell et al. (2003, 2011), Chen et al. (2018) propose a modified fluid factor in which the influence of rock porosity is removed. In this study, we establish a new fluid factor based on the effective model proposed by Hudson et al. (1996), which combines effects of the normal fracture weakness and the pressure relaxation time.

Based on the effective model proposed by Hudson et al. (1996), we simplify and approximate the stiffness matrix of cracked rock in the case of seismic exploration frequency range, and we also express simplified stiffness parameters as a function of dry fracture weaknesses and pressure relaxation related parameter. Using perturbations in the simplified stiffness parameters and relationship between scattering potential and reflection coefficients, we derive a linearized reflection of P-wave incidence and P-wave scattering in the case of on interface separating two cracked layers, from which the corresponding elastic impedance (EI) is also proposed. Based on the derived reflection coefficient, we demonstrate an inversion approach and workflow of employing differences in frequency components of seismic data along two azimuthal angles $\varphi_1 = 0^\circ$ and $\varphi_2 = 90^\circ$ to estimate dry fracture weaknesses and pressure relaxation related parameter. Noisy synthetic seismic data are utilized to testify the stability of the proposed inversion approach. Applying the inversion approach and workflow to real data, we further confirm the stability of our approach, and we also conclude meaningful results relevant to fracture detection and fluid discrimination are generated.

THEORY AND METHOD

Stiffness matrix for rocks with interconnected aligned cracks

In the case of rocks containing a single set of parallel cracks whose normals aligned along the x_1-axis, the stiffness matrix $\mathbf{C}$ is given by (Hudson, 1980; Hudson et al., 1996)

$$\mathbf{C} = \begin{bmatrix} M-\frac{M^2}{\mu}e\widetilde{U_{33}} & \lambda-\frac{\lambda M}{\mu}e\widetilde{U_{33}} & \lambda-\frac{\lambda M}{\mu}e\widetilde{U_{33}} & 0 & 0 & 0 \\ \lambda-\frac{\lambda M}{\mu}e\widetilde{U_{33}} & M-\frac{\lambda^2}{\mu}e\widetilde{U_{33}} & \lambda-\frac{\lambda^2}{\mu}e\widetilde{U_{33}} & 0 & 0 & 0 \\ \lambda-\frac{\lambda M}{\mu}e\widetilde{U_{33}} & \lambda-\frac{\lambda^2}{\mu}e\widetilde{U_{33}} & M-\frac{\lambda^2}{\mu}e\widetilde{U_{33}} & 0 & 0 & 0 \\ 0 & 0 & 0 & \mu & 0 & 0 \\ 0 & 0 & 0 & 0 & \mu-\mu e\widetilde{U_{11}} & 0 \\ 0 & 0 & 0 & 0 & 0 & \mu-\mu e\widetilde{U_{11}} \end{bmatrix}, \tag{1}$$

where $M = \lambda + 2\mu$, e is crack density, λ and μ are Lamé constants of the isotropic and elastic host rock, and $\widetilde{U_{11}}$ and $\widetilde{U_{33}}$ are related to fluid parameters (e.g. fluid viscosity η_{fl}) and crack properties (e.g. crack aspect ratio α). In the case of aligned partially saturated cracks, $\widetilde{U_{11}}$ and $\widetilde{U_{33}}$ are given by (Hudson et al., 1996; Pointer et al., 2000)

$$\widetilde{U_{11}} = \frac{16}{3\,(3-2g)}\frac{1}{1+i\omega\chi}, \widetilde{U_{33}} = \frac{4}{3\,(1-g)}\frac{1}{1+\widetilde{K}}, \tag{2}$$

where $\omega = 2\pi f$ is the angular frequency, $g = \mu/M$, and

$$\begin{aligned} \chi &= \frac{4}{\pi\mu\,(3-2g)}\frac{\eta_{\text{fl}}}{\alpha}, \widetilde{K} = \Psi + i\omega\Gamma, \Psi = \frac{K_{\text{fl}}}{\pi\alpha\mu(1-g)}, \\ \Gamma &= \frac{\eta_{\text{fl}}}{\pi\mu\alpha^3}\frac{F_q}{1-g}, F_q = \frac{0.053(1-q)\left[1+\cos(\pi-q\pi)\right]}{(1-q)^2} \end{aligned} \tag{3}$$

in which η_{fl} is fluid viscosity, α is crack aspect ratio, K_{fl} is the effective bulk modulus of fluid infill, and q is oil saturation in cracks. For cracks that are not too thin (i.e. $\alpha \geq 0.0005$), we observe that in the case that the infill fluid is the mixture of oil and gas Ψ is close to zero because K_{fl} is much smaller than μ, and Γ is the relaxation time affected by aspect ratio and oil saturation and viscosity. Neglecting the effect of Ψ, we proceed to the simplification of $\widetilde{U_{33}}$ and the derivation of the real part of $\widetilde{U_{33}}$

$$\begin{aligned} \Re\left(\widetilde{U_{33}}\right) &= \Re\left[\frac{4}{3\,(1-g)}\frac{1}{1+K}\right] = \Re\left[\frac{4}{3\,(1-g)}\frac{1}{1+i\omega\Gamma}\right] \\ &= \Re\left[\frac{4}{3\,(1-g)}\left(1-i\omega\Gamma_2-\omega^2\Gamma^2+...\right)\right] \approx \frac{4}{3\,(1-g)}\left(1-\omega^2\Gamma^2\right). \end{aligned} \tag{4}$$

Pointer et al. (2000) point out that attenuation and dispersion related to $\widetilde{U_{11}}$ are disregarded in the realm of seismology; hence following Bakulin et al. (2000), we rewrite $\widetilde{U_{11}}$ in the case of fluid filled cracks

$$U_{11} = \frac{16}{3\,(3-2g)}. \tag{5}$$

Given different values of oil saturation q and crack aspect ratio α we first compare the real and imaginary parts of frequency-dependent $\widetilde{U_{33}}$ to confirm feasibility of neglecting the imaginary part in this study. Figure 1 plots comparisons between real and imaginary parts of $\widetilde{U_{33}}$. We observe that $\Re\left(\widetilde{U_{33}}\right)$ is much larger than $\Im\left(\widetilde{U_{33}}\right)$, which proves the imaginary part is negligible in the seismic frequency range.

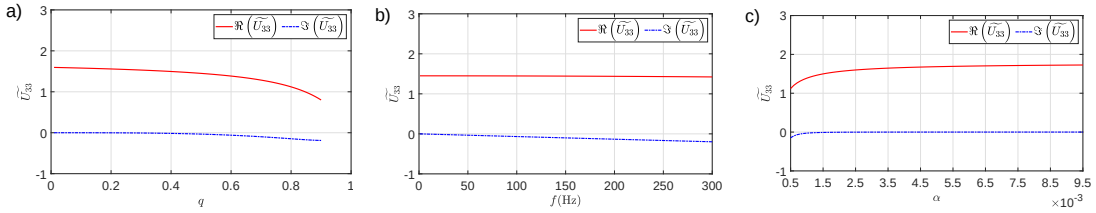

FIG. 1. Comparisons between real and imaginary parts of $\widetilde{U_{33}}$. $\Re\left(\widetilde{U_{33}}\right)$ and $\Im\left(\widetilde{U_{33}}\right)$ represent real and imaginary parts respectively. a) $\widetilde{U_{33}}$ varying with oil-saturation ($\alpha = 0.0005$ and $f = 50$Hz); b) $\widetilde{U_{33}}$ varying with frequency ($\alpha = 0.0005$ and $q = 0.8$); and c) $\widetilde{U_{33}}$ varying with crack aspect ratio ($q = 0.8$ and $f = 50$Hz). Other parameters used in plotting this figure are given by: oil bulk modulus $K_o = 1.5{\times}10^9$Pa and viscosity $\eta_o = 15{\times}10^{-3}$Pa·s, gas bulk modulus $K_g = 0.004 \times 10^9$Pa and viscosity $\eta_g = 0.1{\times}10^{-3}$Pa·s, $\mu = 30{\times}10^9$Pa, and $g = 0.25$.

We next analyze how oil saturation affects parameter Γ in the case of different values of crack aspect ratio, as plotted in Figure 2. We observe that the value of Γ is proportional

to the oil-saturation, which indicates that the inversion result of Γ may be employed as a factor for discriminating oil-bearing reservoirs.

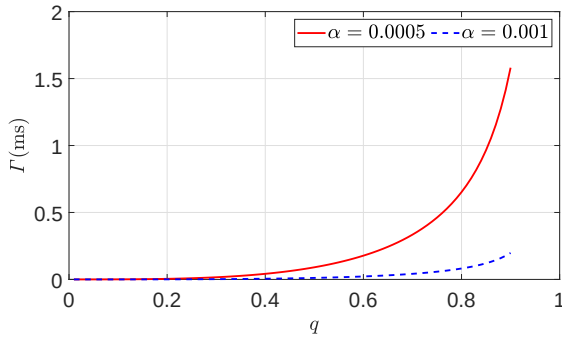

FIG. 2. Variations of Γ with oil saturation. Oil viscosity $\eta_o = 15{\times}10^{-3}$Pa·s, $\mu = 30{\times}10^{9}$Pa, and $g = 0.25$.

Substituting equations 4 and 5 to equation 1, we obtain approximate expressions of stiffness parameters

$$
\begin{aligned}
C_{11} &= M - M\delta_N - \omega^2 M\psi_n, \\
C_{12} &= \lambda - \lambda\delta_N - \omega^2\lambda\psi_n, \\
C_{23} &= \lambda - \lambda(1-2g)\delta_N - \omega^2\lambda(1-2g)\psi_n, \\
C_{33} &= M - \lambda\,(1-2g)\,\delta_N - \omega^2\lambda\,(1-2g)\,\psi_n, \\
C_{44} &= \mu, C_{55} = \mu - \mu\delta_T, \\
C_{13} &= C_{21} = C_{31} = C_{12}, C_{32} = C_{23}, C_{66} = C_{55}, C_{22} = C_{33},
\end{aligned} \tag{6}
$$

where $\psi_n = \delta_N \Gamma^2$, and $\delta_N = \frac{4e}{3g(1-g)}$ and $\delta_T = \frac{16e}{3(3-2g)}$ represent the normal and tangential weaknesses of dry cracks (Bakulin et al., 2000).

Derivation of P-to-P linearized reflection coefficient

Under the assumptions that P-wave incidence angle is small and changes across the reflection interface are small, reflectivity model and volume scattering model are consistent (Moradi and Innanen, 2016). Using stiffness parameters presented in the previous section, we proceed to the derivation of perturbations in the stiffness tensor in the case of an interface separating an two cracked media. For C_{11}, the perturbation ΔC_{11} is expressed as

$$
\begin{aligned}
\Delta C_{11} =& (M + \Delta M) - (M + \Delta M)\,(\delta_N + \Delta\delta_N) - \omega^2\,(M + \Delta M)\,(\psi_n + \Delta\psi_n) \\
&- \left(M - M\delta_N - \omega^2 M\psi_n\right) \\
&\approx \Delta M - \delta_N\Delta M - M\Delta\delta_N - \omega^2 M\Delta\psi_n - \omega^2\psi_n\Delta M,
\end{aligned} \tag{7}
$$

where ΔM, $\Delta\delta_N$ and $\Delta\psi_n$ represent perturbations in M, δ_N and ψ_n across the reflection interface. Again under the assumption of small contrasts across the interface, we neglect

terms those are proportional to $\Delta M\Delta\delta_N$ and $\Delta M\Delta\psi_n$. For other stiffness parameters, their perturbations across the interface are given by

$$\begin{aligned}
\Delta C_{12} \approx& \Delta\lambda - \delta_N\Delta\lambda - \lambda\Delta\delta_N - \omega^2\lambda\Delta\psi_n - \omega^2\psi_n\Delta\lambda,\\
\Delta C_{23} \approx& \Delta\lambda - (1-2g)\delta_N\Delta\lambda - \lambda(1-2g)\Delta\delta_N\\
&- \omega^2\lambda(1-2g)\Delta\psi_n - \omega^2(1-2g)\psi_n\Delta\lambda,\\
\Delta C_{33} \approx& \Delta M - (1-2g)\,\delta_N\Delta\lambda - \lambda\,(1-2g)\,\Delta\delta_N\\
&- \omega^2\lambda\,(1-2g)\,\Delta\psi_n - \omega^2\,(1-2g)\,\psi_n\Delta\lambda,\\
\Delta C_{44} =& \Delta\mu,\\
\Delta C_{55} \approx& \Delta\mu - \delta_T\Delta\mu - \mu\Delta\delta_T,\\
\Delta C_{13} =& \Delta C_{21} = \Delta C_{31} = \Delta C_{12}, \Delta C_{32} = \Delta C_{23},\\
\Delta C_{55} =& \Delta C_{66}, \Delta C_{22} = \Delta C_{33},
\end{aligned} \tag{8}$$

where $\Delta\mu$ and $\Delta\delta_T$ are changes in shear modulus and tangential fracture weakness across the reflection interface. Again under the assumption of small contrasts across the interface, we neglect the term that is proportional to $\Delta\mu\Delta\delta_T$.

The general expression of scattering potential $\mathcal{S}$ is given by (Beylkin and Burridge, 1990; Moradi and Innanen, 2016)

$$\mathcal{S} = \left(\mathcal{P}_{\rm i}\cdot\mathcal{P}_{\rm s}\right)\Delta\rho - \sum_{k=1,l=1}^{k=6,l=6}\xi_{kl}\Delta C_{kl}, \tag{9}$$

where $\mathcal{P}_{\rm i}$ and $\mathcal{P}_{\rm s}$ are respectively the polarization vectors of incidence and scattering waves, which are given by (Shaw and Sen, 2006)

$$\mathcal{P}_{\rm i} = \left[\sin\theta\cos\varphi, \sin\theta\sin\varphi, \cos\theta\right], \mathcal{P}_{\rm s} = \left[-\sin\theta\cos\varphi, -\sin\theta\sin\varphi, \cos\theta\right], \tag{10}$$

where θ is P-wave incidence angle, and φ is the azimuthal angle defined with respected to fracture symmetry. Expressions of ΔC_{kl} are shown in equation 8, and ξ_{kl} are given by (Shaw and Sen, 2006)

$$\begin{aligned}
&\xi_{11} = \frac{\rho\sin^4\theta\cos^4\varphi}{M}, \xi_{12} = \frac{\rho\sin^4\theta\sin^2\varphi\cos^2\varphi}{M}, \xi_{13} = \frac{\rho\sin^2\theta\cos^2\theta\cos^2\varphi}{M}, \xi_{21} = \xi_{12},\\
&\xi_{22} = \frac{\rho\sin^4\theta\sin^4\varphi}{M}, \xi_{23} = \frac{\rho\sin^2\theta\cos^2\theta\sin^2\varphi}{M}, \xi_{31} = \xi_{13}, \xi_{32} = \xi_{23}, \xi_{33} = \frac{\rho\cos^4\theta}{M},\\
&\xi_{44} = \frac{-4\rho\sin^2\theta\cos^2\theta\sin^2\varphi}{M}, \xi_{55} = \frac{-4\rho\sin^2\theta\cos^2\theta\cos^2\varphi}{M}, \xi_{66} = \frac{4\rho\sin^4\theta\sin^2\varphi\cos^2\varphi}{M},
\end{aligned} \tag{11}$$

where ρ is the density of the background rock.

Reflection coefficient for incidence P-wave to scattering P-wave is a scaled version of the scattering potential (Beylkin and Burridge, 1990; Shaw and Sen, 2004; Moradi and Innanen, 2016), which is given by

$$R_{\rm PP} = \frac{1}{4\rho\cos^2\theta}\mathcal{S}. \tag{12}$$

Combining equations 7-12, we derive the linearized P-to-P reflection coefficient as (Appendix A)

$$\begin{aligned} R_{\mathrm{PP}}(\theta,\varphi,\omega) =& \frac{\cos 2\theta}{2\cos^2\theta} R_\rho + \frac{1}{2\cos^2\theta} R_M - 4g\sin^2\theta R_\mu \\ & - \frac{1}{4\cos^2\theta}\left[1-2g\left(\sin^2\theta\sin^2\varphi+\cos^2\theta\right)\right]^2 \Delta\delta_N \\ & - \frac{\omega^2}{4\cos^2\theta}\left[1-2g\left(\sin^2\theta\sin^2\varphi+\cos^2\theta\right)\right]^2 \Delta\psi_n \\ & + g\left(\sin^2\theta\cos^2\varphi - \sin^2\theta\tan^2\theta\sin^2\varphi\cos^2\varphi\right)\Delta\delta_T, \end{aligned} \tag{13}$$

where $R_M = \frac{\Delta M}{2M}$, $R_\mu = \frac{\Delta\mu}{2\mu}$, and $R_\rho = \frac{\Delta\rho}{2\rho}$ represent reflectivities of P- and S-wave moduli and density, respectively.

Using the derived reflection coefficient, we further express the difference of the P-wave reflection coefficient at the azimuthal angles $\varphi_1 = 0^\circ$ and $\varphi_2 = 90^\circ$ as

$$\begin{aligned} \delta R_{\mathrm{PP}}(\theta,\omega) =& R_{\mathrm{PP}}(\theta,\varphi_1=0^\circ,\omega) - R_{\mathrm{PP}}(\theta,\varphi_2=90^\circ,\omega) \\ =& \frac{1}{4\cos^2\theta}\left[(1-2g)^2 - \left(1-2g\cos^2\theta\right)^2\right]\Delta\delta_N \\ & + \frac{\omega^2}{4\cos^2\theta}\left[(1-2g)^2 - \left(1-2g\cos^2\theta\right)^2\right]\Delta\psi_n \\ & + g\sin^2\theta\Delta\delta_T, \end{aligned} \tag{14}$$

where $\delta R_{\mathrm{PP}}(\theta,\omega)$ is the frequency-dependent reflection coefficient difference, which also varies with the incidence angle.

We construct a three-layer model plotted in Figure 3(a) to compute differences between reflection coefficients using the derived equations. Table 1 shows elastic parameters (P- and S-wave moduli and density) of isotropic background rocks, and values of crack density and oil saturation for different layers. Figure 3(b) plots comparisons between variations of reflection coefficient differences with the incidence angle in the case of different frequencies ($f_1 = 10\mathrm{Hz}$, $f_2 = 25\mathrm{Hz}$ and $f_3 = 40\mathrm{Hz}$). The computed reflection coefficient differences shown in Figure 3(b) and Ricker wavelets whose dominant frequencies are consistent with those used for compute reflection coefficients are employed to generate seismic amplitude differences, as plotted in Figure 3(c). Crack properties and fluid parameters are given by $\alpha = 0.0005$, $K_o = 1.5\mathrm{GPa}$, $\eta_o = 15\times10^{-3}\mathrm{Pa{\cdot}s}$, $K_g = 0.004\mathrm{GPa}$, and $\eta_g = 0.1\times10^{-3}\mathrm{Pa{\cdot}s}$.

Table 1. Elastic parameters, crack density, and oil saturation for different layers

	$M(\mathrm{GPa})$	$\mu(\mathrm{GPa})$	$\rho(\mathrm{g/cm^3})$	e	q
L1(Shale)	20.4	4.04	2.43	0.001	0.02
L2(Sand)	23.3	6.31	2.28	0.1	0.7
L3(Sand)	23.3	6.31	2.28	0.05	0.3

From Figure 3 we observe that differences in reflection coefficients increase with the incidence angle, and in the case of a fixed incidence angle the absolute value of difference in

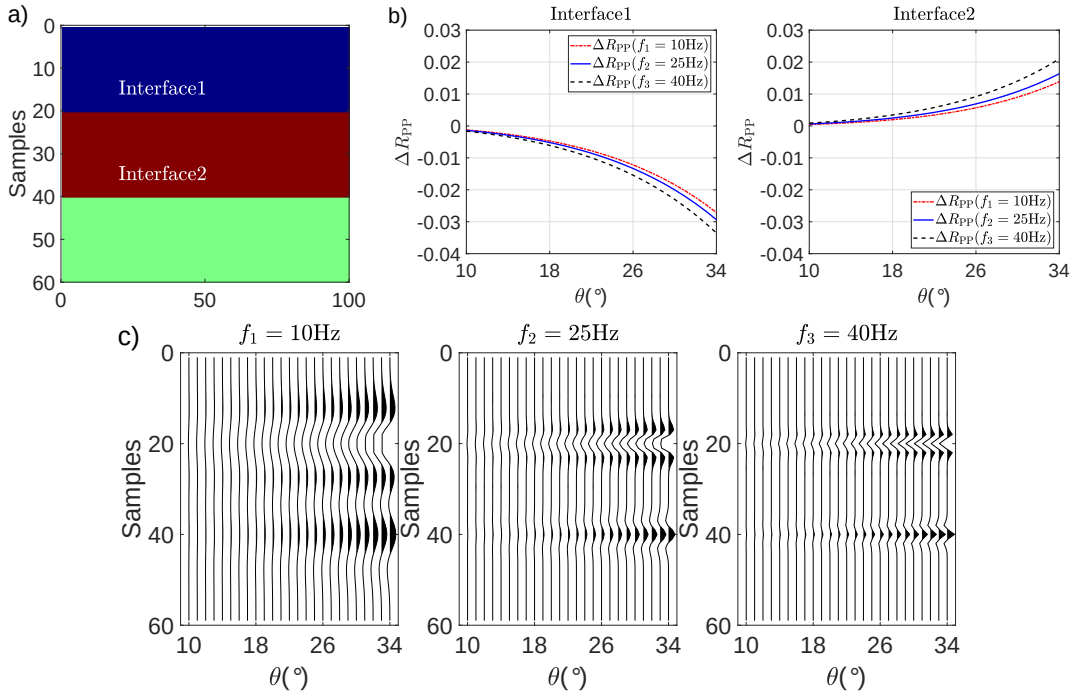

FIG. 3. a) Three-layer model; b) Comparisons between reflection coefficient differences of different frequencies; and c) Comparisons between seismic amplitude differences of different frequencies.

reflection coefficient increase with the frequency. From differences in seismic amplitudes, we conclude that the influence of wavelet should be removed first to provide frequency-dependent reflection coefficient differences.

Following the azimuthal EI given by Chen et al. (2018), we present the expression of Quasi-difference in Elastic Impedance ($Q\delta\mathrm{EI}$)

$$\begin{aligned}\delta R_{\mathrm{PP}}(\theta,\omega) =& R_{\mathrm{PP}}(\theta,\varphi_1=0^\circ,\omega) - R_{\mathrm{PP}}(\theta,\varphi_2=90^\circ,\omega)\\ =& \frac{1}{2}d\left[\ln\mathrm{EI}(\theta,\varphi_1=0^\circ,\omega)\right] - \frac{1}{2}d\left[\ln\mathrm{EI}(\theta,\varphi_2=90^\circ,\omega)\right]\\ =& \frac{1}{2}d\left[\ln\frac{\mathrm{EI}(\theta,\varphi_1=0^\circ,\omega)}{\mathrm{EI}(\theta,\varphi_2=90^\circ,\omega)}\right] = \frac{1}{2}d\left[\ln(Q\delta\mathrm{EI})\right].\end{aligned} \tag{15}$$

Following Martins (2006), we rewrite equation 14 under the assumption of θ and ω being constant quantities as

$$\begin{aligned}2\delta R_{\mathrm{PP}}(\theta,\omega) =& d[\ln(Q\delta\mathrm{EI})]\\ =& \frac{1}{2\cos^2\theta}\left[(1-2g)^2 - \left(1-2g\cos^2\theta\right)^2\right](d\delta_N)\\ &+ \frac{\omega^2}{2\cos^2\theta}\left[(1-2g)^2 - \left(1-2g\cos^2\theta\right)^2\right](d\psi_n)\\ &+ 2g\sin^2\theta(d\delta_T),\end{aligned} \tag{16}$$

where $d\delta_N \approx \Delta\delta_N$, $d\psi_n \approx \Delta\psi_n$, and $d\delta_T \approx \Delta\delta_T$, which are approximated under the assumption of continuous variation of medium properties.

Combining equations 15 and 16, and taking integral of δR_{PP} yields

$$\begin{aligned} 2\int \delta R_{\mathrm{PP}} =& \int d\left[\ln(Q\delta \mathrm{EI})\right] \\ =& \frac{1}{2\cos^2\theta}\left[(1-2g)^2-\left(1-2g\cos^2\theta\right)^2\right]\int (d\delta_N) \\ &+\frac{\omega^2}{2\cos^2\theta}\left[(1-2g)^2-\left(1-2g\cos^2\theta\right)^2\right]\int (d\psi_n) \\ &+2g\sin^2\theta\int (d\delta_T), \end{aligned} \tag{17}$$

We stress that in the selected time window g is also considered to be a constant when we compute the value of $Q\delta\mathrm{EI}$. After some algebra we obtain the expression of $\ln Q\delta\mathrm{EI}$ in terms of δ_N, δ_T and ψ_n

$$\ln(Q\delta\mathrm{EI}) = P_{\delta_N}(\theta,g)\,\delta_N + P_{\psi_n}(\theta,\omega,g)\,\psi_n + P_{\delta_T}(\theta,g)\,\delta_T, \tag{18}$$

where

$$\begin{aligned} P_{\delta_N}(\theta,g) &= \frac{1}{2\cos^2\theta}\left[(1-2g)^2-\left(1-2g\cos^2\theta\right)^2\right], \\ P_{\psi_n}(\theta,\omega,g) &= \frac{\omega^2}{2\cos^2\theta}\left[(1-2g)^2-\left(1-2g\cos^2\theta\right)^2\right], \\ P_{\delta_T}(\theta,g) &= 2g\sin^2\theta. \end{aligned} \tag{19}$$

Inversion of differences in seismic amplitudes for dry rock weaknesses and pressure relaxation related parameter

Based on the derived reflection coefficient and the obtained expression of $\ln(Q\delta\mathrm{EI})$, we proceed to the estimation of dry fracture weaknesses and pressure relaxation related parameter using frequency components of seismic amplitude differences variation with the incidence angle. We first implement the estimation of $\ln\mathrm{EI}(\varphi_1=0^\circ)$ and $\ln\mathrm{EI}(\varphi_2=90^\circ)$ utilizing different frequency components of seismic data along azimuthal angles $\varphi_1=0^\circ$ and $\varphi_2=90^\circ$, from which we may compute the $\ln Q\delta\mathrm{EI}$. Using the computed $\ln Q\delta\mathrm{EI}$, we finally implement the inversion for dry fracture weaknesses and pressure relaxation related parameter. Figure 4 plots the workflow of implementing the inversion for dry fracture weaknesses and pressure relaxation related parameter.

We next explain how to implement the inversion for $\ln\mathrm{EI}$ using input seismic data. Relationship between seismic data and $\ln\mathrm{EI}$ is given by (Chen et al., 2018)

$$\mathbf{S} = \mathbf{AX} = \frac{1}{2}\mathbf{WDLEI}, \tag{20}$$

where

$$\mathbf{A} = \frac{1}{2}\mathbf{WD}, \mathbf{X} = \mathbf{LEI},$$

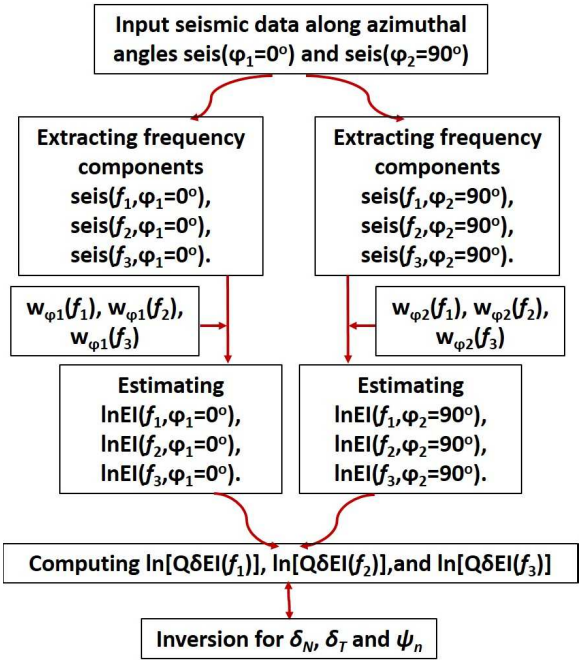

FIG. 4. Workflow of inversion for dry fracture weaknesses and pressure relaxation related parameter. Quantities $\mathrm{w}_{\varphi_1}(f_1)$, $\mathrm{w}_{\varphi_1}(f_2)$ and $\mathrm{w}_{\varphi_1}(f_3)$ and quantities $\mathrm{w}_{\varphi_2}(f_1)$, $\mathrm{w}_{\varphi_2}(f_2)$ and $\mathrm{w}_{\varphi_2}(f_3)$ denote wavelets extracted from corresponding seismic data of azimuthal angle $\varphi_1 = 0°$ and $\varphi_2 = 90°$ respectively.

$$\mathbf{S} = \begin{bmatrix} s(t_1,\theta,\varphi) \\ \vdots \\ s(t_l,\theta,\varphi) \end{bmatrix}_{l\times 1}, \mathbf{W} = \begin{bmatrix} \mathrm{w}_1 & 0 & \dots & 0 \\ \mathrm{w}_2 & \mathrm{w}_1 & \ddots & \vdots \\ \vdots & \vdots & \ddots & 0 \\ \mathrm{w}_l & \mathrm{w}_{l-1} & \dots & \mathrm{w}_1 \end{bmatrix}_{l\times l},$$

$$\mathbf{D} = \begin{bmatrix} -1 & 1 & & \\ & -1 & 1 & \\ & & \ddots & \ddots \\ & & & -1 \ \ 1 \end{bmatrix}_{l\times(l+1)}, \mathbf{LEI} = \begin{bmatrix} \ln \mathrm{EI}(t_1,\theta,\varphi) \\ \vdots \\ \ln \mathrm{EI}(t_{l+1},\theta,\varphi) \end{bmatrix}_{(l+1)\times 1}, \tag{21}$$

in which $t_1, ..., t_{l+1}$ represent all the interfaces, and $\mathrm{w}_1, ..., \mathrm{w}_l$ represent samples of the extracted wavelet. In the inversion for $\ln \mathrm{EI}$, values of azimuthal angle ϕ are given by $\varphi_1 = 0°$ and $\varphi_2 = 90°$ respectively, and the incidence angle θ is respectively replaced with three different angles θ_1, θ_2 and θ_3. The damped least-squares inversion algorithm is employed to obtain results of **LEI** (Chen et al., 2018).

With the estimated results of $\ln \mathrm{EI}$ in hand, we first compute values of $\ln Q\delta\mathrm{EI}$, and then we implement the inversion for δ_N, ψ_n and δ_T. In the case of A

$$\mathbf{d} = \mathbf{Gm}, \tag{22}$$

where

$$\mathbf{d} = \begin{bmatrix} \mathbf{LQEI}(\theta_1,\omega_1) \\ \mathbf{LQEI}(\theta_2,\omega_1) \\ \mathbf{LQEI}(\theta_3,\omega_1) \\ \mathbf{LQEI}(\theta_1,\omega_2) \\ \mathbf{LQEI}(\theta_2,\omega_2) \\ \mathbf{LQEI}(\theta_3,\omega_2) \\ \mathbf{LQEI}(\theta_1,\omega_3) \\ \mathbf{LQEI}(\theta_2,\omega_3) \\ \mathbf{LQEI}(\theta_3,\omega_3) \end{bmatrix}_{9(l+1)\times 1}, \mathbf{G} = \begin{bmatrix} \mathbf{P}_{\delta_N}(\theta_1) & \mathbf{P}_{\psi_n}(\theta_1,\omega_1) & \mathbf{P}_{\delta_T}(\theta_1) \\ \mathbf{P}_{\delta_N}(\theta_2) & \mathbf{P}_{\psi_n}(\theta_2,\omega_1) & \mathbf{P}_{\delta_T}(\theta_2) \\ \mathbf{P}_{\delta_N}(\theta_3) & \mathbf{P}_{\psi_n}(\theta_3,\omega_1) & \mathbf{P}_{\delta_T}(\theta_3) \\ \mathbf{P}_{\delta_N}(\theta_1) & \mathbf{P}_{\psi_n}(\theta_1,\omega_2) & \mathbf{P}_{\delta_T}(\theta_1) \\ \mathbf{P}_{\delta_N}(\theta_2) & \mathbf{P}_{\psi_n}(\theta_2,\omega_2) & \mathbf{P}_{\delta_T}(\theta_2) \\ \mathbf{P}_{\delta_N}(\theta_3) & \mathbf{P}_{\psi_n}(\theta_3,\omega_2) & \mathbf{P}_{\delta_T}(\theta_3) \\ \mathbf{P}_{\delta_N}(\theta_1) & \mathbf{P}_{\psi_n}(\theta_1,\omega_3) & \mathbf{P}_{\delta_T}(\theta_1) \\ \mathbf{P}_{\delta_N}(\theta_2) & \mathbf{P}_{\psi_n}(\theta_2,\omega_3) & \mathbf{P}_{\delta_T}(\theta_2) \\ \mathbf{P}_{\delta_N}(\theta_3) & \mathbf{P}_{\psi_n}(\theta_3,\omega_3) & \mathbf{P}_{\delta_T}(\theta_3) \end{bmatrix}_{9(l+1)\times 3(l+1)},$$

$$\mathbf{m} = \begin{bmatrix} \boldsymbol{\delta}_N \\ \boldsymbol{\psi}_n \\ \boldsymbol{\delta}_T \end{bmatrix}_{3(l+1)\times 1},$$

$$\boldsymbol{\delta}_N = \begin{bmatrix} \delta_N(t_1) \\ \vdots \\ \delta_N(t_{l+1}) \end{bmatrix}_{(l+1)\times 1}, \boldsymbol{\psi}_N = \begin{bmatrix} \psi_n(t_1) \\ \vdots \\ \psi_n(t_{l+1}) \end{bmatrix}_{(l+1)\times 1}, \boldsymbol{\delta}_T = \begin{bmatrix} \delta_T(t_1) \\ \vdots \\ \delta_T(t_{l+1}) \end{bmatrix}_{(l+1)\times 1},$$

$$\mathbf{LQEI} = \begin{bmatrix} \ln Q\delta\mathrm{EI}(t_1) \\ \vdots \\ \ln Q\delta\mathrm{EI}(t_{l+1}) \end{bmatrix}_{(l+1)\times 1}, \mathbf{P}_{\delta_N}(\theta) = \begin{bmatrix} P_{\delta_N}(\theta,g_1) & & \\ & \ddots & \\ & & P_{\delta_N}(\theta,g_{l+1}) \end{bmatrix}_{(l+1)\times(l+1)},$$

$$\mathbf{P}_{\delta_T}(\theta) = \begin{bmatrix} P_{\delta_T}(\theta,g_1) & & \\ & \ddots & \\ & & P_{\delta_T}(\theta,g_{l+1}) \end{bmatrix}_{(l+1)\times(l+1)},$$

$$\mathbf{P}_{\psi_n}(\theta,\omega) = \begin{bmatrix} P_{\psi_n}(\theta,\omega,g_1) & & \\ & \ddots & \\ & & P_{\psi_n}(\theta,\omega,g_{l+1}) \end{bmatrix}_{(l+1)\times(l+1)}. \tag{23}$$

In order to obtain the inversion results of δ_N, ψ_n and δ_T, we make probabilistic estimates of the unknown parameter vector $\mathbf{m}$ based on Bayes' theorem. The posterior probability distribution function $P(\mathbf{m}|\mathbf{d})$ is related to the likelihood function $P(\mathbf{d}|\mathbf{m})$ and a priori probability function $P(\mathbf{m})$

$$P(\mathbf{m}|\mathbf{d}) \propto P(\mathbf{d}|\mathbf{m})\, P(\mathbf{m}). \tag{24}$$

Assuming the noise to be Gaussian with variance σ_n (Downton, 2005), we obtain the likelihood function as

$$P(\mathbf{d}|\mathbf{m}) = \frac{1}{\sigma_n\sqrt{2\pi}}\exp\left[-\frac{(\mathbf{d}-\mathbf{G}\mathbf{m})^{\dagger}(\mathbf{d}-\mathbf{G}\mathbf{m})}{2\sigma_n^2}\right], \tag{25}$$

where $\dagger$ denotes the transpose of matrix. Given mean $\mathbf{m}_{\text{prior}}$ and given covariance $\mathbf{C_m}$ (Tarantola, 2005), we again assume the priori model follows Gaussian distribution

$$P(\mathbf{m}) = \frac{\exp\left[-\frac{1}{2}(\mathbf{m}-\mathbf{m}_{\text{prior}})^{\dagger}\mathbf{C}_{\mathbf{m}}^{-1}(\mathbf{m}-\mathbf{m}_{\text{prior}})\right]}{\sqrt{2\pi}\sqrt{\det(\mathbf{C_m})}}. \tag{26}$$

Combining equations 24-26, we write the posterior probability distribution function as

$$P(\mathbf{m}|\mathbf{d}) \propto \frac{1}{\sigma_n 2\pi\sqrt{\det(\mathbf{C_m})}}\exp[-J(\mathbf{m})], \tag{27}$$

where

$$\begin{aligned} J(\mathbf{m}) &= \frac{(\mathbf{d}-\mathbf{G}\mathbf{m})^{\dagger}(\mathbf{d}-\mathbf{G}\mathbf{m})}{2\sigma_n^2} + \frac{(\mathbf{m}-\mathbf{m}_{\text{prior}})^{\dagger}(\mathbf{m}-\mathbf{m}_{\text{prior}})}{2\mathbf{C_m}}, \\ \mathbf{C_m} &= \begin{bmatrix} \sigma_{\delta_N}^2 & \sigma_{\delta_N\psi_n} & \sigma_{\delta_N\delta_T} \\ \sigma_{\delta_N\psi_n} & \sigma_{\psi_n}^2 & \sigma_{\psi_n\delta_T} \\ \sigma_{\delta_N\delta_T} & \sigma_{\psi_n\delta_T} & \sigma_{\delta_T}^2 \end{bmatrix}, \end{aligned} \tag{28}$$

in which $\sigma_{\delta_N}^2$, $\sigma_{\psi_n}^2$ and $\sigma_{\delta_T}^2$ are variances of δ_N, ψ_n and δ_T, and other diagonal elements are related to the variance and the correlation coefficient (e.g. $\sigma_{\delta_N\delta_T} = r_{\delta_N\delta_T}\sigma_{\delta_N}\sigma_{\delta_T}$, where $r_{\delta_N\delta_T}$ is the correlation coefficient between δ_N and δ_T).

In order to obtain the maximum posterior probability, we should search for the minimum of the function $J(\mathbf{m})$, which requires the derivative of $J(\mathbf{m})$ with respect to $\mathbf{m}$ to be zero. Hence the solution of $\mathbf{m}$ is given by (Tarantola, 2005)

$$\mathbf{m} = \mathbf{m}_{\text{prior}} + \left(\mathbf{G}^{\dagger}\sigma_n^{-2}\mathbf{G} + \mathbf{C}_{\mathbf{m}}^{-1}\right)^{-1}\mathbf{G}^{\dagger}\mathbf{C}_{\mathbf{m}}^{-1}\left(\mathbf{d} - \mathbf{G}\mathbf{m}_{\text{prior}}\right). \tag{29}$$

NUMERICAL EXPERIMENTS

Synthetic tests

We first construct a fractured well log model to testify the proposed approach. We employ well log data (P- and S-wave velocities and density) to compute P- and S-wave moduli of isotropic background, as plotted in Figure 5(a). The model of fracture density e is shown in Figure 5(b), and In Figure 5(b), we also plot the model of oil saturation parameter q. Using the oil saturation, we calculate results of pressure relaxation time Γ. We next compute results of dry fracture weaknesses δ_N and δ_T and pressure relaxation related parameter ψ_n, which are displayed in Figure 5(c). We observe that the results of δ_N and δ_T are consistent with values of fracture density, which indicates that δ_N and δ_T are valuable quantities to be employed for the prediction of fractures, and we also see the results of ψ_n are sensitive to oil saturation.

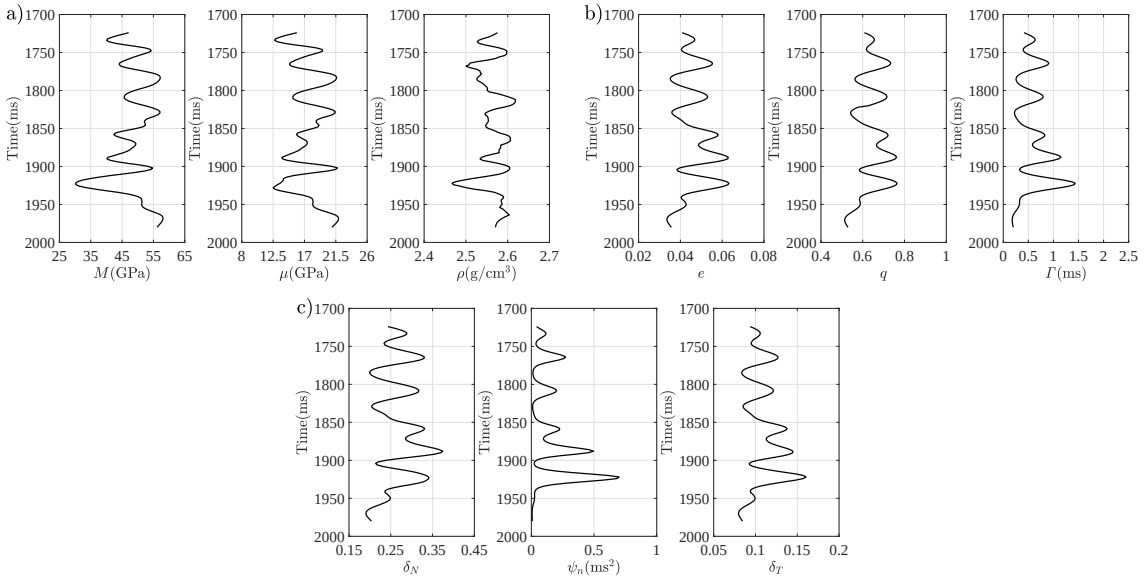

FIG. 5. Constructed a fractured well log model.

We next utilize Ricker wavelet of dominate frequencies $f_1 = 10$Hz, $f_2 = 25$Hz and $f_3 = 40$Hz and corresponding reflection coefficients calculated using the derived equations to generate synthetic seismic data given azimuthal angles $\varphi_1 = 0^\circ$ and $\varphi_2 = 90^\circ$ and P-wave incidence angle θ range 1°-34°. Taking CDP 400 as an example of inversion test first, we plot differences between generated synthetic seismic data along azimuthal angles φ_1 and φ_2 at different frequencies in Figure 6, and Figure 6(a) and 6(b) respectively represent the case of no noise included in the synthetic data and the case of adding Gaussian random

noise with a signal-to-noise ratio (SNR) of 3 into the synthetic data. From the differences in synthetic seismic data we observe more obvious seismic amplitude residuals exhibiting at fractured layers with relatively large values of δ_T and ψ_n.

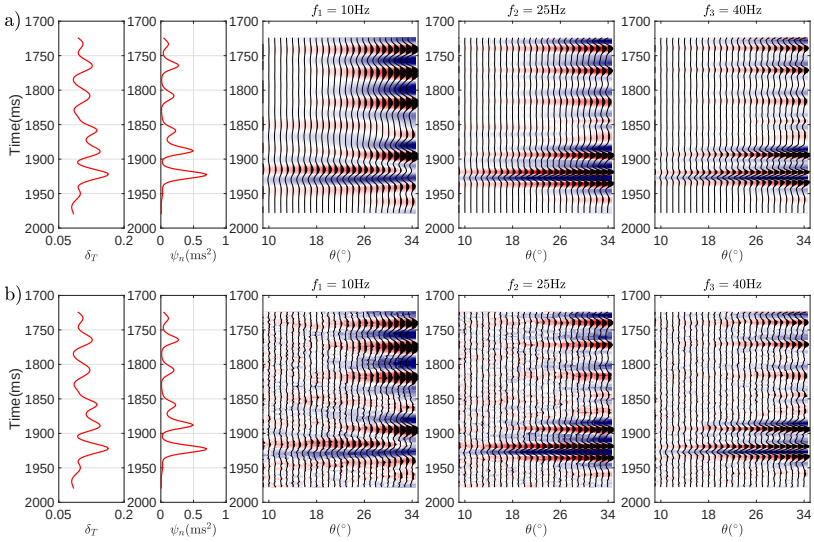

FIG. 6. Differences in synthetic seismic data along different azimuthal angles $\varphi_1 = 0^\circ$ and $\varphi_2 = 90^\circ$ in the case of different frequencies. a) No noise added into synthetic data, b) Adding Gaussian random noise with a SNR of 3 into synthetic data.

Using the proposed approach, we first implement the inversion for $\ln Q\delta EI$, and comparisons between true values of $\ln Q\delta EI$ calculated using equation 18 and inversion results are plotted in Figure 7. We observe the inversion results match the true values well even in the case of SNR of 3, which verifies that the estimated results of $\ln Q\delta EI$ can be used for subsequent inversion for dry fracture weaknesses and pressure relaxation related parameter. Using the estimated results of $\ln Q\delta EI$, we next implement the inversion for δ_N, ψ_n and δ_T, and comparisons between true values and inversion results of δ_N, ψ_n and δ_T are plotted in Figure 8. We observe that in the case of no noise added in the synthetic data there is a good match between the true value and the inversion result, especially for δ_N and δ_T, and in the case of SNR of 3 we may also obtain the acceptable inversion results, which confirms the stability and robustness of the proposed inversion approach.

Example of real data test

We finally utilize a real data set to further confirm the reliability of the proposed inversion approach and workflow. The real data are acquired above a oil-bearing reservoir, and the data have been processed and sampled in different azimuths and offsets. P-wave velocity provided by well-log data is employed to transfer seismic data from offset domain to incidence angle domain, which is implemented using a commercial software package. The data also underwent amplitude versus incidence angle and azimuth (AVAZ) compliant preprocessing prior to being used in the present study, and modification of observation azimuth (i.e. the azimuthal angle represents difference between fracture symmetry azimuth and observation azimuth). We utilize pre-stack seismic data of one Inline along two different azimuthal angles ($\varphi_1 = 0^\circ$ and $\varphi_2 = 90^\circ$) to testify the proposed inversion method.

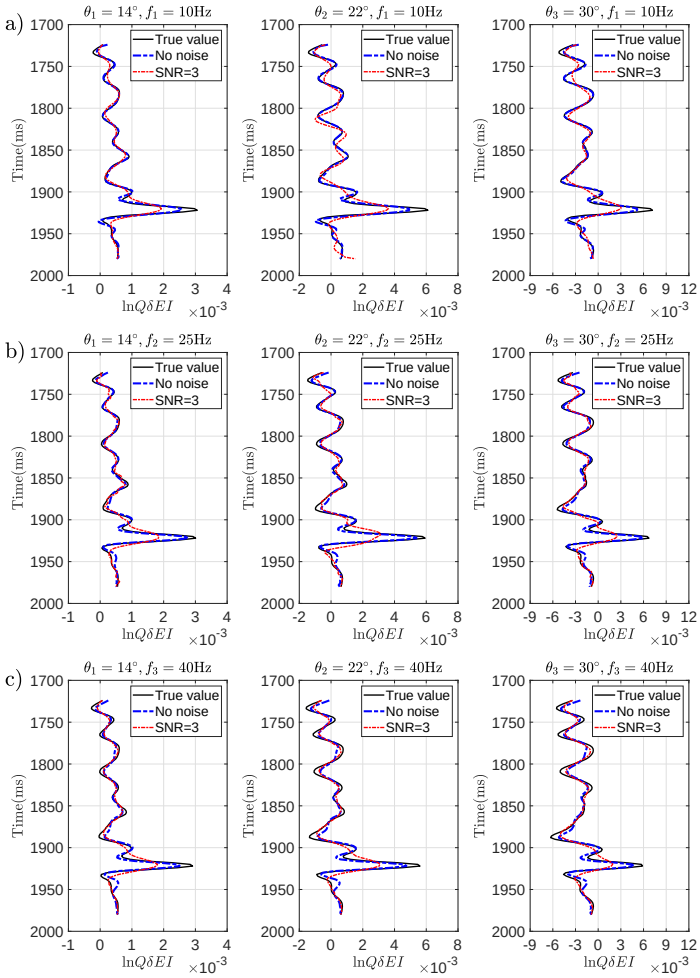

FIG. 7. Comparisons between true values and inversion results of $\ln Q\delta EI$. a) f_1=10Hz, b) f_2=25Hz, and c) f_3=40Hz.

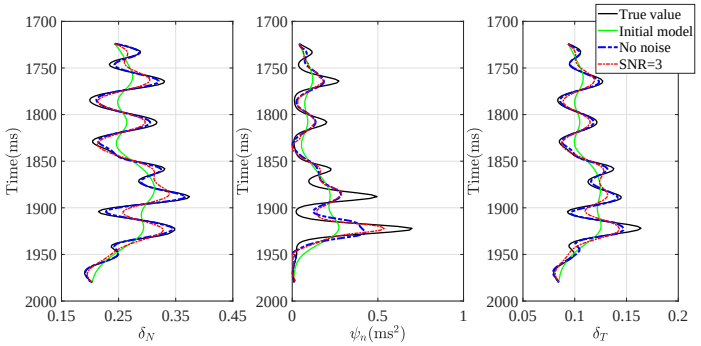

FIG. 8. Comparisons between true values and inversion results of δ_N, ψ_n and δ_T. Green curve represents initial model, which is a smoothed version of the corresponding true value.

Figure 9 (a) and (b) plot seismic angle gathers extracted at the location of well log along azimuths φ_1 and φ_2, and differences between the angle gathers along two azimuths are shown in Figure 9(c). The ellipses in Figure 9 indicates the location of oil reservoir. We observe that there is a pronounced AVA phenomenon around the location of oil reservoir, and from the spliced P-wave velocity we observe the oil reservoir exhibits low values of velocity.

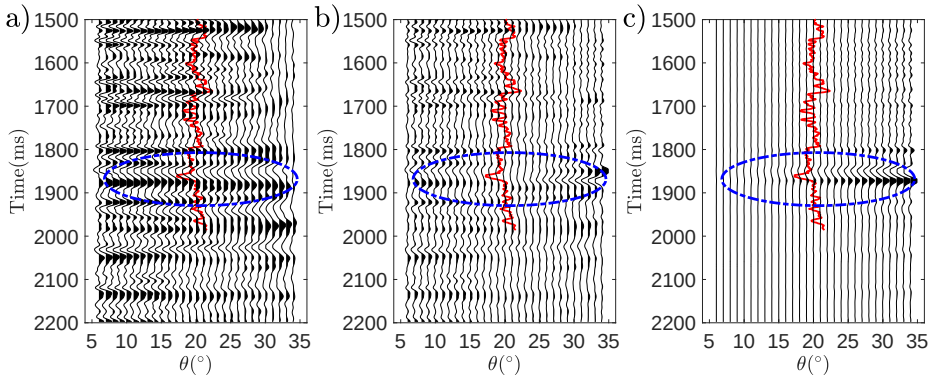

FIG. 9. Seismic angle gathers extracted at the location of well log. a) $\varphi_1 = 0°$, b) $\varphi_2 = 90°$, and c) differences between these two angle gathers. The curve indicates P-wave velocity.

Figure 10 plots stacked profiles of the Inline along azimuths φ_1 and φ_2 respectively, and we also display differences between these two stacked profiles. From the differences between stacked seismic data along azimuths φ_1 and φ_2 we observe that around the location of fractured reservoir there are strong reflection amplitudes remain.

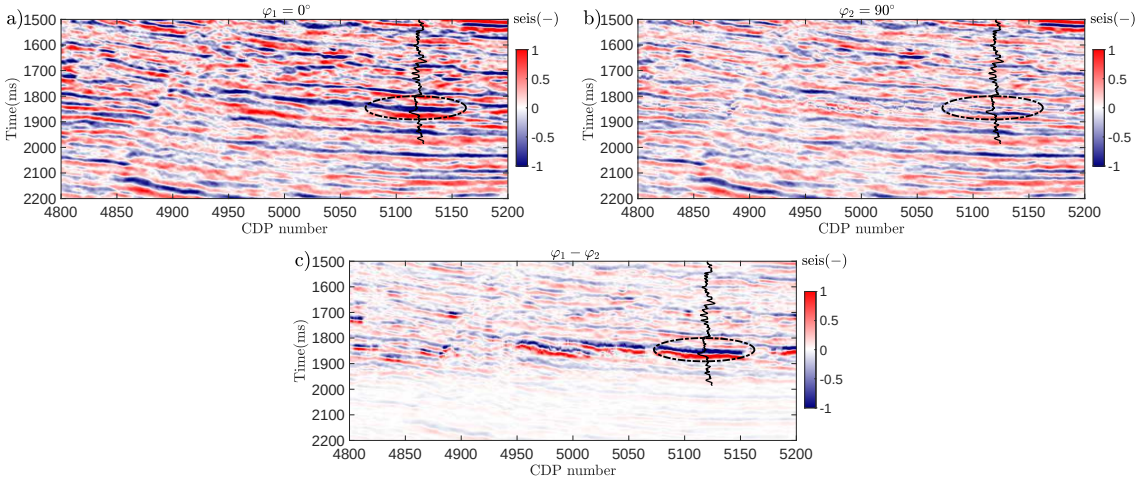

FIG. 10. Stacked seismic profiles. a) $\varphi_1 = 0°$, b) $\varphi_2 = 90°$, and c) differences between these two seismic profiles. The curve indicates P-wave velocity, and the ellipses indicates the location of oil reservoir.

Following the proposed inversion workflow, we next extract different components of seismic data and obtain incidence-angle-stacked seismic data that are partially stacked over different incidence angle ranges (i.e. data of central angle $\theta_1 = 14°$ are stacked using pre-stack data of angle $10° - 18°$; data of central angle $\theta_2 = 22°$ stacked using pre-stack data of angle $18° - 26°$; and data of central angle $\theta_3 = 30°$ stacked using pre-stack data of angle $26° - 34°$), as plotted in Figure 11. We stress that the frequency components are extracted using different rectangle filters in frequency domain.

Using seismic data plotted in Figure 11 and the corresponding extracted wavelets, we implement the estimation of EI using the least-squares inversion algorithm, and the inversion results of EI are plotted in Figure 12.

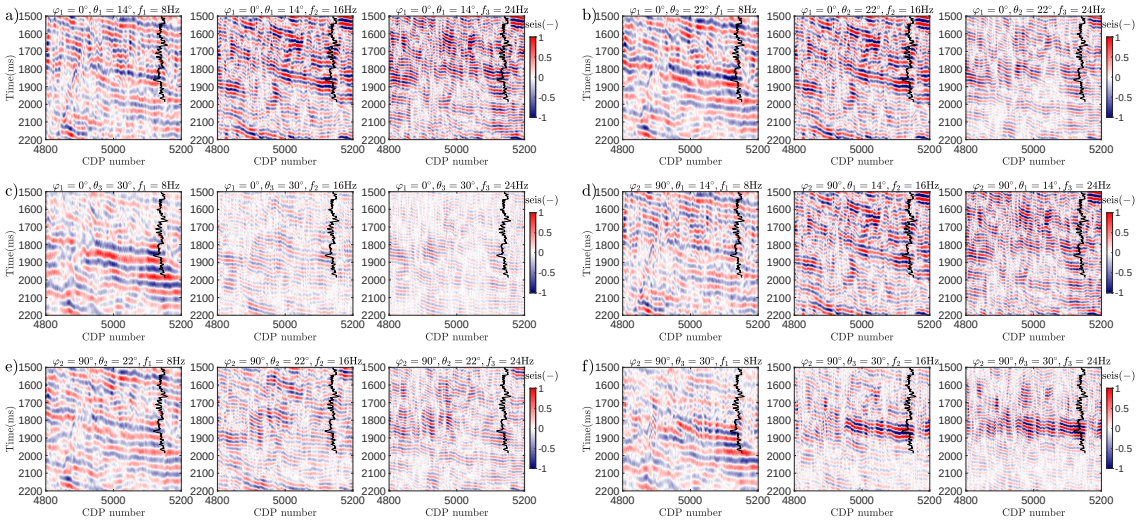

FIG. 11. Different frequency components of incidence-angle-stacked seismic data. a) $\varphi_1 = 0°$, $\theta_1 = 14°$; b) $\varphi_1 = 0°$, $\theta_2 = 22°$; c) $\varphi_1 = 0°$, $\theta_3 = 30°$; d) $\varphi_2 = 90°$, $\theta_1 = 14°$; e) $\varphi_2 = 90°$, $\theta_2 = 22°$; and f) $\varphi_2 = 90°$, $\theta_3 = 30°$.

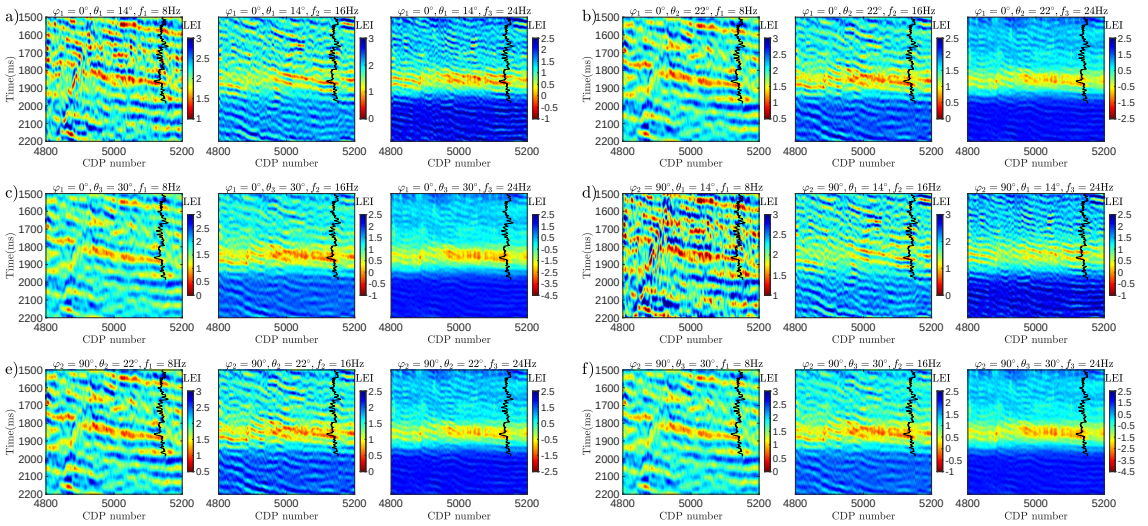

FIG. 12. Results of LEI estimated from different frequency components of incidence-angle-stacked seismic data. a) $\varphi_1 = 0°$, $\theta_1 = 14°$; b) $\varphi_1 = 0°$, $\theta_2 = 22°$; c) $\varphi_1 = 0°$, $\theta_3 = 30°$; d) $\varphi_2 = 90°$, $\theta_1 = 14°$; e) $\varphi_2 = 90°$, $\theta_2 = 22°$; and f) $\varphi_2 = 90°$, $\theta_3 = 30°$.

From Figure 12 we observe that around the location of oil reservoir the inversion results of LEI show low values, which are consistent with P-wave velocity, and the oil bearing reservoirs become more distinct in the estimated LEI of a relatively high frequency. Using the inverted LEI, we may compute results of $\ln Q\delta EI$ and implement the inversion for δ_N, ψ_n and δ_T. Figure 13 plots the inversion results of dry fracture weaknesses and pressure relaxation related parameter. We observe that at the location of fractured reservoirs the inversion results of δ_N, ψ_n and δ_T exhibit relatively high values, and we also see the distinction between fractured reservoir (especially oil-bearing fractured reservoir) and non-fractured reservoir in the inversion result of pressure relaxation related parameter is more obvious than that in the inversion results of dry fracture weaknesses, which reveals the estimated pressure relaxation related parameter can be preserved as an additional and

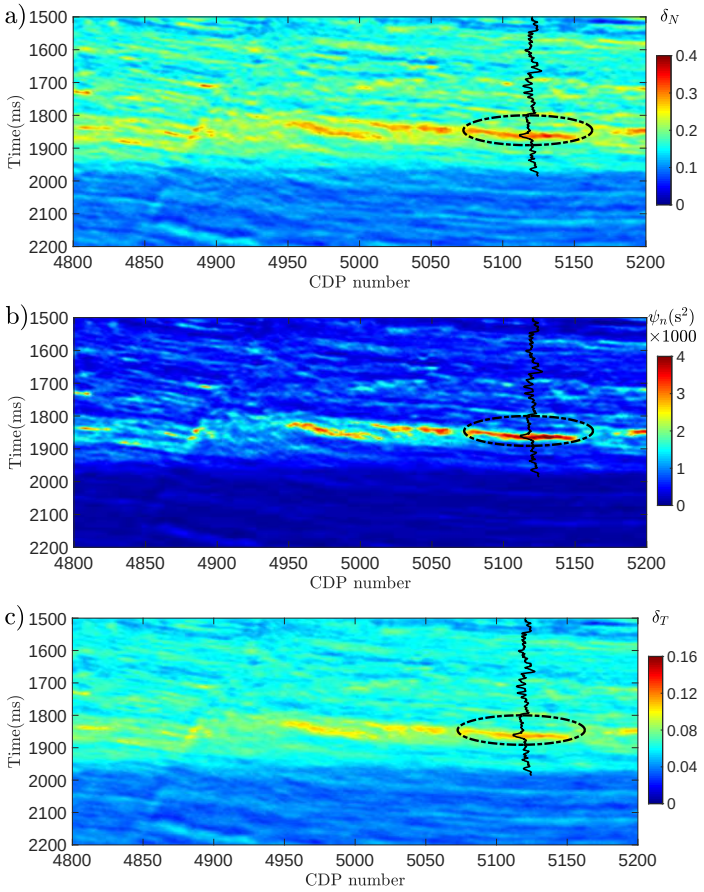

FIG. 13. Inversion results of dry fracture weaknesses and pressure relaxation related parameter. The ellipse indicates the location of oil-bearing fractured reservoir, and the curve represents P-wave velocity.

valuable proof for distinguish oil-bearing fractured reservoirs.

CONCLUSIONS

Based on an attenuative cracked effective model, we first simplify and approximate the parameters that are related to fluid properties (fluid saturation, bulk modulus and viscosity), from which we present three variables (dry fracture weaknesses and pressure relaxation related parameter) that are sensitive to dry fractures and fluids. Using stiffness matrix of rocks that contain a set of aligned and partially saturated cracks, which is frequency-dependent and expressed as a function of the presented three variables, we obtain perturbations in all stiffness parameters in the case of one reflection interface separating two fractured rocks. Utilizing the obtained perturbations and the relationship between scattering potential and reflection coefficient, we derive a linearized reflection coefficient of P-wave incidence and P-wave scattering in terms of dry fracture weaknesses and pressure relaxation related parameter.

Based on the derived reflection coefficient, we establish an inversion workflow and approach to estimate dry fracture weaknesses and pressure relaxation related parameter from frequency components of amplitude differences in seismic data along two azimuthal

angles $\varphi_1 = 0^\circ$ and $\varphi_2 = 90^\circ$. The established inversion workflow involves two steps: 1) estimating Quasi-difference in Elastic Impedance ($Q\delta EI$) from inversion results of Elastic Impedance (EI) estimated from frequency components of partially incidence-angle-stacked seismic data along azimuthal angles φ_1 and φ_2, and 2) predicting dry fracture weaknesses and pressure relaxation related parameter from the estimated results of $Q\delta EI$ using an inversion algorithm established based on Bayes' theorem. The stability of the proposed inversion approach is confirmed using synthetic seismic data in the presence of moderate random noise. Applying the proposed inversion approach and workflow to a real data set acquired above a oil-bearing fractured reservoir and processed to meet requirements of azimuthal amplitude inversion (e.g. azimuthal angle modification, transferring data from offset domain to incidence angle domain, amplitude versus incidence angle and azimuth compliant processing), we conclude that our approach appears to provide additional and valuable results that can be used to identify oil-bearing fracture reservoirs.

In order to apply the proposed inversion approach and workflow, we should pay attention to some conditions and assumptions under which we derive the linearized reflection coefficient and establish the inversion approach, which includes: 1) The frequency-dependent stiffness matrix is derived in the case of rocks containing a set of parallel cracks that are vertical or sub-vertical and partially saturated, which emphasizes fractured/cracked reservoirs are filled with fluids that are mixture of gas and oil or mixture of gas and water; 2) in the derivation of stiffness matrix we consider the case of a small crack density ($e \leq 0.01$) and not too thin cracks (i.e. $\alpha \geq 0.0005$), which allows us to reasonably neglect the imaginary part of stiffness parameters; and 3) when deriving the linearized reflection coefficient, we assume perturbations of P- and S-wave moduli across the interface are small, which requires cracks/fractures are embedded in the rock rather than being distributed at rock interface locations of different types of lithology. These assumptions and conditions, to some extent, restrict the applicability of the derived reflection coefficient and the proposed inversion approach; however, oil-bearing carbonate rock reservoirs in which vertical or sub-vertical cracks exist fall into this category.

ACKNOWLEDGMENTS

The industrial sponsors of the Consortium for Research in Elastic Wave Exploration Seismology (CREWES) are thanked for their support. We gratefully acknowledge additional support from Natural Science and Engineering Research Council of Canada through the grant no. CRDPJ 461179-13. This research was undertaken thanks in part to funding from the Canada First Research Excellence Fund, and the Mitacs Accelerate grant *Responsible Development of Unconventional Hydrocarbon Reserves*. The SINOPEC Key Lab of Multi-Component Seismic Technology is thanked for providing the processed real data. Hampson-Russell software was used for wavelet extraction and transferring seismic data from offset domain to incidence angle domain.

APPENDIX A. DERIVATION OF LINEARIZED REFLECTION COEFFICIENT FOR P-WAVE INCIDENCE AND P-WAVE SCATTERING

Substituting equations 7-11 into equation 12, we obtain

$$R_{\rm PP} = \frac{1}{4\rho\cos^2\theta}S = \frac{1}{4\rho\cos^2\theta}\begin{bmatrix}\Delta\rho\cos2\theta+\Delta C_{11}\xi_{11}+\Delta C_{12}(\xi_{12}+\xi_{21})+\Delta C_{13}(\xi_{13}+\xi_{31})\\ +\Delta C_{22}\xi_{22}+\Delta C_{23}(\xi_{23}+\xi_{32})+\Delta C_{33}\xi_{33}\\ +\Delta C_{44}\xi_{44}+\Delta C_{55}\xi_{55}+\Delta C_{66}\xi_{66}\end{bmatrix}. \tag{A.1}$$

After some algebra we derive the linearized reflection coefficient as

$$\begin{aligned} R_{\rm PP}(\theta,\varphi,\omega) =& \frac{\cos2\theta}{2\cos^2\theta}R_\rho + \frac{1}{2\cos^2\theta}R_M - 4g\sin^2\theta R_\mu \\ &- \frac{1}{4\cos^2\theta}\left[1-2g\left(\sin^2\theta\sin^2\varphi+\cos^2\theta\right)\right]^2\Delta\delta_N \\ &- \frac{\omega^2}{4\cos^2\theta}\left[1-2g\left(\sin^2\theta\sin^2\varphi+\cos^2\theta\right)\right]^2\Delta\psi_n \\ &+ g\left(\sin^2\theta\cos^2\varphi-\sin^2\theta\tan^2\theta\sin^2\varphi\cos^2\varphi\right)\Delta\delta_T, \end{aligned} \tag{A.2}$$

where $R_M = \frac{\Delta M}{2M}$, $R_\mu = \frac{\Delta\mu}{2\mu}$, and $R_\rho = \frac{\Delta\rho}{2\rho}$ represent reflectivities of P- and S-wave moduli and density, respectively. We stress that in the derivation of reflection coefficient we neglect terms those are proportional to $R_M\delta_N$, $R_\mu\delta_N$ and $R_\mu\delta_T$ under the assumption of small contrasts in P- and S-wave moduli across reflection interfaces.

REFERENCES

Bakulin, A., Grechka, V., and Tsvankin, I., 2000, Estimation of fracture parameters from reflection seismic data—part i: Hti model due to a single fracture set: Geophysics, **65**, No. 6, 1788–1802.

Beylkin, G., and Burridge, R., 1990, Linearized inverse scattering problems in acoustics and elasticity: Wave motion, **12**, No. 1, 15–52.

Carcione, J. M., 2000, A model for seismic velocity and attenuation in petroleum source rocksan acoustic model for petroleum source rocks: Geophysics, **65**, No. 4, 1080–1092.

Carcione, J. M., 2007, Wave fields in real media: Wave propagation in anisotropic, anelastic, porous and electromagnetic media, vol. 38: Elsevier.

Chapman, M., Liu, E., and Li, X.-Y., 2006, The influence of fluid sensitive dispersion and attenuation on avo analysis: Geophysical Journal International, **167**, No. 1, 89–105.

Chen, H., Ji, Y., and Innanen, K. A., 2018, Estimation of modified fluid factor and dry fracture weaknesses using azimuthal elastic impedance: Geophysics, **83**, No. 1, WA73–WA88.

Downton, J. E., 2005, Seismic parameter estimation from avo inversion: Ph.D. thesis, University of Calgary.

Goodway, B., 2001, Avo and lamé constants for rock parameterization and fluid detection: CSEG Recorder, **26**, No. 6, 39–60.

Gurevich, B., 2003, Elastic properties of saturated porous rocks with aligned fractures: Journal of Applied Geophysics, **54**, No. 3-4, 203–218.

Hudson, J., 1980, Overall properties of a cracked solid: Mathematical Proceedings of the Cambridge Philosophical Society, **88**, No. 2, 371–384.

Hudson, J., Liu, E., and Crampin, S., 1996, The mechanical properties of materials with interconnected cracks and pores: Geophysical Journal International, **124**, No. 1, 105–112.

Martins, J. L., 2006, Elastic impedance in weakly anisotropic media: Geophysics, **71**, No. 3, D73–D83.

Moradi, S., and Innanen, K. A., 2016, Viscoelastic amplitude variation with offset equations with account taken of jumps in attenuation angle: Geophysics, **81**, No. 3, N17–N29.

Pointer, T., Liu, E., and Hudson, J. A., 2000, Seismic wave propagation in cracked porous media: Geophysical Journal International, **142**, No. 1, 199–231.

Russell, B. H., Gray, D., and Hampson, D. P., 2011, Linearized avo and poroelasticity: Geophysics, **76**, No. 3, C19–C29.

Russell, B. H., Hedlin, K., Hilterman, F. J., and Lines, L. R., 2003, Fluid-property discrimination with avo: A biot-gassmann perspective: Geophysics, **68**, No. 1, 29–39.

Schoenberg, M., and Sayers, C. M., 1995, Seismic anisotropy of fractured rock: Geophysics, **60**, No. 1, 204–211.

Shaw, R. K., and Sen, M. K., 2004, Born integral, stationary phase and linearized reflection coefficients in weak anisotropic media: Geophysical Journal International, **158**, No. 1, 225–238.

Shaw, R. K., and Sen, M. K., 2006, Use of avoa data to estimate fluid indicator in a vertically fractured medium: Geophysics, **71**, No. 3, C15–C24.

Tarantola, A., 2005, Inverse problem theory and methods for model parameter estimation: siam.

Zimmer, M. A., 2003, Seismic velocities in unconsolidated sands: Measurements of pressure, sorting, and compaction effects: Ph.D. thesis, Stanford University.